Chapter 8

Summary and future directions

8.1 Summary of experimental findings

A combination of modern surface science techniques (CAICISS, LEED and XPS), has been used to investigate the atomic structure of clean metal single crystal surfaces, and changes to the structure and composition of the near-surface region following the adsorption of oxygen and platinum. Specifically, the clean Cu(100) and Pt(111) surfaces have been investigated, along with the adsorption of O on Pt(111) and Ni(110), and the deposition of Pt on the Cu(100), Ni(110)-(3×1)-O and NiO(110) surfaces. This chapter summarizes the experimental work presented in the preceding chapters, as well as identifying potential experiments, outstanding theoretical issues and potential improvements to the experimental setup.

8.1.1 Oxidation of the Pt(111) surface

Following the application of standard IBA procedures to clean the Pt(111) surface, a (1×1) LEED pattern and a contaminant-free XPS spectrum were observed. Analysis of the CAICISS data taken in the $< \bar{2}11>$ and $<110>$ azimuths revealed a 2% expansion in the outermost interlayer spacing, Δ_{12}, along with a 6% expansion in Δ_{23}. In addition, every second atom in the surface layer was found to lie 0.1 Å below the level of its nearest neighbour.

Previous work on the oxidation of Pt surfaces with molecular oxygen (O_2) indicated that a saturation coverage of just 0.25 ML could be achieved. In an attempt to increase the oxygen saturation coverage, the Pt(111) surface was exposed to an atomic oxygen beam. A series of short exposures to atomic oxygen were monitored with LEED, with a p(2×2) LEED pattern observed after a 5.0 L exposure. Further exposure to atomic oxygen saw the background of the LEED pattern increase until no

spots were discernable after a total exposure of 50 L.

Investigations of the surface following a 50 L exposure were carried out using CAICISS and XPS. Analysis of the O 1*s* and Pt 4*f* regions of the XPS spectrum revealed two components due to on-surface oxygen atoms and oxygen atoms contained within a Pt-oxide layer. This result provides evidence that the use of atomic oxygen leads to an increase in the saturation coverage of oxygen on the Pt(111) surface. Further analysis with XPS data taken at a range of take-off angles led to the calculation of a 1.3 ML total oxygen coverage after a 50 L exposure. Analysis of CAICISS data taken from this surface revealed the smoothing of the features in the first $\sim 40^{\circ}$ of the Pt-backscattered intensity profile. This was due to disruption in the surface layer due to O adsorption, in agreement with the increase of the background intensity of the LEED pattern. Features at low polar angles in the CAICISS spectrum were found to be indicative of a substitutional oxide, as opposed to O atoms residing in interstitial sites. The on-surface O atoms were found to reside in three-fold hollow sites.

Throughout, the exposure times of O-covered surfaces to both ion and electron beams were limited. Electron-stimulated desorption was seen in LEED after a period of ~ 10 minutes, whilst ion-stimulated desorption was limited by the slight misalignment of the polar rotation axis with respect to the incident beam to induce a movement of the beam spot across the surface during the experiment.

The O-saturated surface was then annealed to 500°C and sharp p(2×2) reconstruction with low background intensity was observed. In addition, the features corresponding to the Pt-oxide layer in the O 1*s* and Pt 4*f* regions were also removed. These observations, in conjunction with the CAICISS data recorded from the surface, suggested a re-ordering of the surface and the elimination of the sub-surface oxide on annealing.

8.1.2 Pt deposition on the Cu(100) surface

The structure of the clean Cu(100) surface and the characteristics of Pt deposition on the surface up to a coverage of 2.75 ML, as well as the effects of subsequent annealing of the sample, were investigated.

The Cu(100) surface was prepared using IBA and a (1×1) LEED pattern and a contamination-free XPS spectrum were observed. CAICISS data were then taken in the <100> and <110> azimuths, and analysis of these data, using the FAN simulation software, revealed relaxations in the surface region. The outermost interlayer spacing, Δ_{12}, was found to have contracted by $\sim$ 4%, whilst second interlayer spacing, Δ_{23}, was found to have expanded by $\sim$ 1%. Such relaxations are generally expected from clean metal surfaces, with the relaxations observed in the near-surface region of the Cu(100) structure agreeing with previous observations [12, 185].

The room temperature deposition of Pt on Cu(100) led to the presence of sub-surface Pt atoms at total coverage of just 0.25 ML, most probably in an effort to lower the surface energy of the system. Expansions in the interlayer spacings in the near-surface region with respect to the clean surface structure were also observed due to the inclusion of the larger Pt atoms in the Cu(100) structure during the formation of a Cu-Pt alloy. A weak c(2×2) LEED pattern was observed, indicating some degree of order at the surface. However, increased background relative to the clean surface indicated some degree of disorder induced by the Pt deposition.

Continued Pt deposition led to the surface region comprising a majority of Pt atoms. However, Cu atoms were still present in the surface layer up to Pt coverages of approximately 2.0 ML. As the Pt coverage increased, a small Pt overlayer was observed on the surface in addition to a purely Pt surface layer, but no LEED patterns were observed during this stage. All experimental observations supported the formation of a disordered Pt film on top of a Cu-Pt alloy structure at coverages in excess of approximately 2.0 ML.

Following the deposition of 2.75 ML of Pt, the sample was annealed to 300°C for 10 minutes. This led to the restoration of a weak c(2×2) LEED pattern. The notion that some ordering had occurred was also supported by the sharpening of the peaks in the Pt-backscattered intensity profile. Analysis of the features contained within the profile led to the conclusion that the surface now had an average 1:1 compositional ratio of Cu and Pt atoms. The second layer was found to be of Cu_2Pt composition, whilst the remaining layers within the CAICISS probing depth were found to have an

average Cu_3Pt composition. This indicates the significant diffusion of Pt into the bulk Cu(100) lattice during the annealing process.

8.1.3 Pt deposition on oxygen-covered Ni(110) surfaces

During this investigation, the following systems were studied:

- The structure of the Ni(110)-(3×1)-O surface.
- Room temperature deposition of Pt on the Ni(110)-(3×1)-O surface.
- The oxidation of the Ni(110) surface.
- Deposition of Pt on the NiO(110) surfaces.

Following a 1.0 L oxygen exposure, LEED and CAICISS were used to determine that a (3×1)-O structured overlayer had been formed, with the rows of O atoms occupying every third row in the <100> direction, corresponding to a total O coverage of 1/3 ML. This was found to induce relaxations in the surface region, with a $\sim$ 7% expansion in Δ_{12} and a $\sim$ 4% expansion in Δ_{23}. It was also found that the (3×1)-O layer was $\sim$ 1.0 Å above the outermost layer of the Ni(110) structure.

The initial stage of Pt deposition on the Ni(110)-(3×1)-O surface saw the addition of 0.30 ML of Pt to the surface. No LEED pattern was observed. CAICISS data acquired after the Pt deposition indicated the existence of sub-surface Pt atoms and hence the formation of a Ni-Pt alloy structure. Further deposition of Pt led to an extension of the alloy film deeper into the Ni(110) structure, with expansions in the interlayer spacings but no concrete evidence of the onset of layer-by-layer growth of a Pt film on the surface.

A series of short oxygen doses were applied to the clean Ni(110) surface, with the (3×1)-O added row, the (2×1)-O and the (3×1)-O missing row structures observed using LEED following exposures of 1.0 L, 1.5 L and 3.0 L respectively. Further exposure to oxygen led to an increase in the background intensity of the LEED pattern, indicating disorder in the surface region as a result of the O adsorption.

The level of oxygen exposure was increased to 1800 L, with atomic oxygen used to increase the efficiency of oxidation. This led to the formation of a thick NiO(110) film, with CAICISS and LEED data indicating a disordered surface layer. 0.31 ML of Pt was deposited on to this surface at room temperature. In this case, several features were observed within the CAICISS and XPS data which indicated the formation of a Pt overlayer on top of the NiO film, and hence a change in the growth mode with respect to Pt deposition on the clean Ni(110) surface. A similar situation was found at a Pt coverage of 0.80 ML, with no features observed which would indicate the existence of sub-surface Pt atoms. However, annealing at 400°C for 10 minutes saw the elimination of the NiO structure and the diffusion of Pt atoms into the near-surface region in order to form a Ni-Pt alloy.

8.2 Future studies

In addition to the essential investigation of the correction factor outlined in section 8.3, it may also be interesting to investigate the effect of oxidising the Cu(100) surface prior to Pt deposition. Oxidation of the Ni(110) surface led to an immediate switch from alloy formation to layer-by-layer growth at sub-monolayer Pt coverages. This may also be the case for Pt deposition on oxidised Cu(100). It would also be interesting to investigate the deposition of Pt on the Ni(100) surface in order to compare the findings with those presented here on the Cu(100) surface. Other materials could be co-adsorbed with Pt to act as surfactants, again in an effort to produce well-ordered Pt films on top of the Cu(100) and Ni(110) structures. Lastly, InN(0001) surfaces have been briefly studied, a topic outlined in more detail below and one which merits further investigation in the future. More generally, the work carried out in the last few years illustrates that CAICISS can be applied to a wide range of materials provided that a crystalline surface can be prepared to a suitable standard and the constituent elements have a sufficient mass difference to be resolved in the ToF data.

8.2.1 Study of InN(0001) surfaces

InN films [200–211] have been identified for potential applications in many areas, particularly in novel high collection efficiency solar cells [202, 203], and so it is important to understand the results of RF-MBE growth in terms of the polarity of the material grown. A second issue in this field is the removal of atmospheric contaminants from the surface which are adsorbed on extraction from the growth chamber. To investigate these problems, CAICISS was used to determine the polarity of InN films grown at Cornell and Ritsumeikan Universities. In addition, XPS, HREELS and SEM were used to study the effects of atomic hydrogen cleaning of InN surfaces.

The bulk of the previous direct polarity determination of InN films has been performed using techniques other than ion scattering. Araki *et al.* used a combination of TEM and CBED to study their RF-MBE grown N-polarity material [212]. Using SEM, the same group have also used a KOH solution to distinguish differences in the wet etching of In-polarity and N-polarity material [213]. Meanwhile, Nanishi and co-workers have used XRD, TEM, EXAFS and Raman scattering to characterise their N-polarity InN films [214]. The majority of this work on InN polarity determination has been carried out *in-situ* (i.e. within the growth chamber). The work detailed below discusses the *ex-situ* cleaning and analysis of InN films grown at Cornell and Ritsumeikan Universities. A combination of HREELS, LEED, XPS, SEM, AFM and CAICISS have been used to study the surfaces at Warwick.

Cleaning of InN surfaces following transportation from the growth chamber is non-trivial, with the surfaces being susceptible to significant structural and electronic damage [215] and prone to the formation of In droplets on the surface [216]. The surfaces cannot be annealed to high temperature as the dissociation temperature of InN is lower than that of the native oxide species, In_2O_3 [36]. Similarly, IBA recipes cannot be used as bombardment with heavy ions leads to the preferential sputtering of N atoms, leaving an In-rich surface [35].

An earlier attempt to clean InN surfaces by AHC was performed by Ohashi and co-workers [36]. This work indicated that atomic hydrogen exposures up to approximately 4 kL could remove a portion of the native oxides in the surface region. A thermal gas

cracker with a $H_2 \rightarrow H^*$ cracking efficiency of approximately 1.5% was used. However, a non-negligible concentration of In_2O_3 remained, indicating that the surface had not been exposed to sufficient atomic hydrogen.

The initial AHC process employed at Warwick consisted of three stages, using the OAR TC-50 thermal gas cracker ($\sim$ 50% cracking efficiency for H_2). The first stage saw the surface exposed to 8 kL of cracked H_2 at 300 K, followed by a second 8 kL exposure at 450 K. Finally, the surface was annealed at 575 K for 2 hours in pressures below 1×10^{-8} mbar. This procedure was carried out on samples R799 (Ritsumeikan University) and GS1532 (Cornell University). The LEED patterns shown in figure 8.1 were taken from the samples at the completion of the AHC process. Both LEED patterns show a (1×1) reconstruction of the InN surface, with the relatively low background intensity indicating a well-ordered surface in each case.

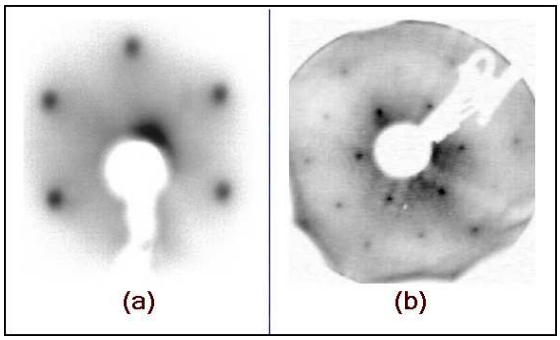

Figure 8.1: LEED patterns recorded following the completion of the AHC process from samples (a) R799 (InN(000$\bar{1}$) at 79.5 eV and (b) GS1532 (InN(0001)) at 168 eV.

The effectiveness of the AHC process was also studied using HREELS, with the data taken from sample GS1532 before and after the AHC process presented elsewhere [215]. Briefly, prior to cleaning, the vibrational modes due to In-O and C-H bonds were clearly present at energy losses of $\sim$ 100 meV, $\sim$ 170 meV and $\sim$ 360 meV [217]. Following the AHC process, the FWHM of the elastic peak (centered at 0 eV) was reduced from 39 meV to 12 meV. The vibrational modes due to surface contamination were no longer present, indicating that the AHC process had produced a clean InN surface. Indeed, the phonon and plasmon peaks were visible in the post-AHC HREELS data, corresponding well with values previously obtained from clean InN surfaces [209].

Sample GS1532 was also studied using XPS, with the full data and analysis presented elsewhere [215]. In brief, the pre-AHC O 1*s* peak showed the existence of both on-surface hydroxides and In_2O_3. The spectra clearly showed the severe reduction in the concentration of oxides and hydrocarbons in the surface region to a much higher degree than that achieved by Ohashi [36]. Inspection of the In 3*d* and N 1*s* regions revealed a similar story. A large concentration of In_2O_3 was observed on the high binding energy side of both the $3d_{5/2}$ and $3d_{3/2}$ peaks prior to cleaning. These components were removed by the AHC process, indicating that the surface had been cleaned effectively. However, closer inspection of the surface with XPS using a range of take-off angles revealed an increase in the In/N ratio with decreasing take-off angle, indicating an In-rich surface. Quantitative analysis of the data taken at a TOA of 45° showed an In/N ratio of 2.8±0.7, significantly higher than the ratio of 1 which would be expected for a stoichiometric surface region. This ratio increased still further as the XPS data became more surface specific, indicating that the excess In region is reasonably well confined to the surface.

The CAICISS data recorded in the <1000> azimuth from samples GS1532 and R799 are shown in figures 8.2 and 8.3 respectively. In the GS1532 case, simulations of these data using the FAN software revealed a In-polarity film, whilst a N-polarity film was found in the R799 case. However, both spectra contain a feature at a polar angle of 60° which was found to be due to the existence of pure In islands, up to 4 ML high, on top of the InN surface [218].

With the production of In islands, the initial AHC recipe had to be adjusted in order to form a clean, stoichiometric surface. Firstly, a recipe with higher temperatures was used and saw the sample exposed to 16 kL of cracked H_2 at 550 K, followed by annealing at 550 K for 1 hour in pressures below 1×10^{-8} mbar. However, the AFM and SEM data recorded from sample R799, shown in figure 8.4, illustrate that this method led to the formation of extremely large metallic In droplets on the surface, some in excess of 200 nm in height. A similar result was found on an In-polarity sample (GS1469).

A second attempt to modify the cleaning recipe saw the implementation of a more

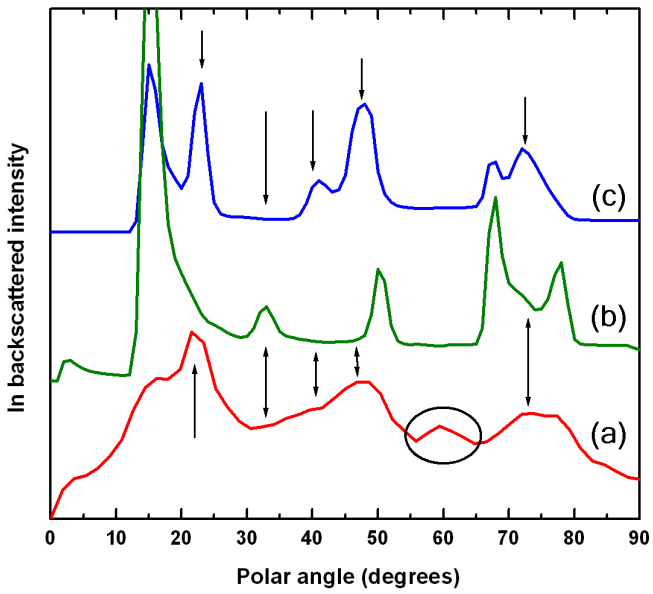

Figure 8.2: (a) CAICISS data collected from sample GS1532 (InN(0001)) in the <1000> direction. (b) shows the simulation of the bulk InN($000\bar{1}$) structure (N-polarity), whilst (c) shows the simulation of the bulk InN(0001) structure (In-polarity). The arrows highlight peaks more accurately described by the In-polarity model, whilst the circled peak at 59° is due to regions of metallic In on the surface.

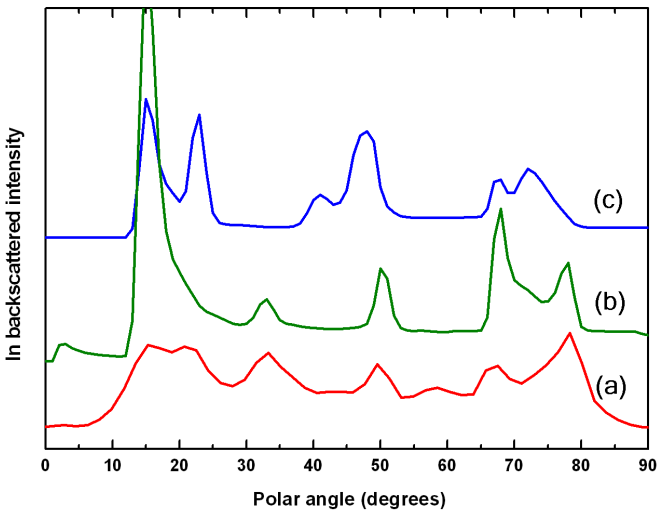

Figure 8.3: (a) CAICISS data collected from sample R799 (InN($000\bar{1}$)) in the <1000> direction. (b) shows the corresponding simulation of the bulk InN($000\bar{1}$) structure (N-polarity), whilst (c) shows the simulation of the bulk InN(0001) structure (In-polarity).

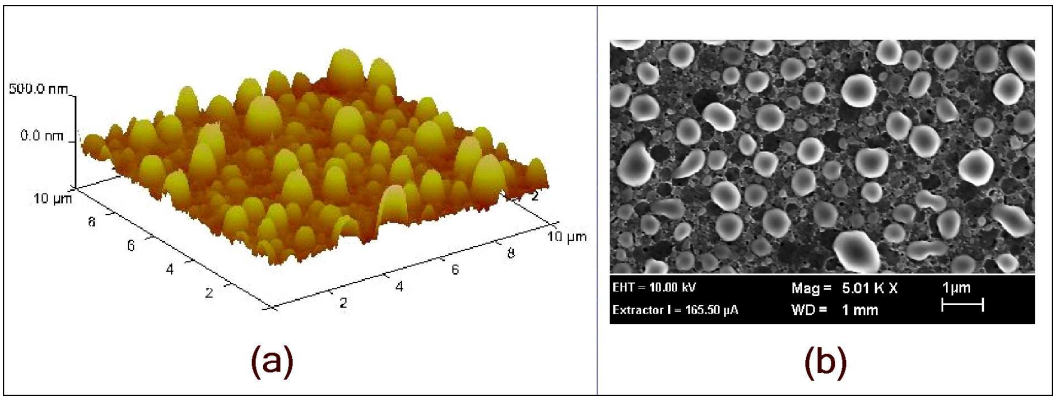

Figure 8.4: (a) AFM and (b) SEM data collected from sample R799 (InN(000$\bar{1}$)) following the AHC process. Both images show the formation of large In droplets on the surface, with droplet heights in excess of 200 nm.

gradual approach, with lower H* exposures and annealing temperatures being used. Firstly, the surface was exposed to a 2.7 kL cracked H_2 dose at 498.5 K, followed by annealing for 30 minutes at 463 K. The surface was then exposed to a 3.6 kL cracked H_2 dose at 463 K and a 4.5 kL cracked H_2 dose at 473 K. Finally, the sample was annealed at 543 K for 30 minutes in pressures below 1×10^{-8} mbar. AFM and SEM images, shown in figure 8.5 provided evidence of a relatively flat surface, free from In droplets, following the application of this AHC recipe to sample GS1409. With

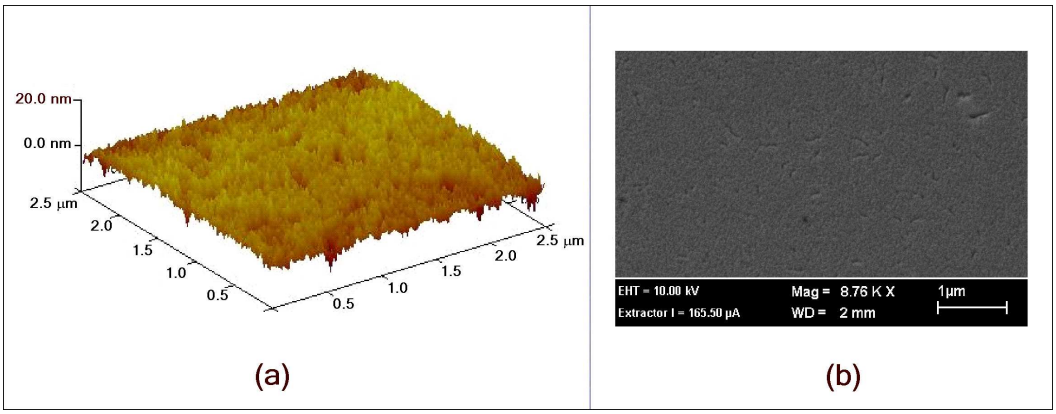

Figure 8.5: (a) AFM and (b) SEM data collected from sample GS1409 (InN(0001)) following the completion of the revised AHC process. Both images show the absence of In droplets on the surface, indicating that this particular AHC has successfully produced a clean, flat, stoichiometric InN surface.

this recipe in place, a more complete study of the structure and composition of InN surfaces using CAICISS and XPS will be possible in the future. If the AHC recipe is successful, a full structural study of the surface of both In-polarity and N-polarity material could be carried out. On a similar theme, the surface of GaN(0001) films could also be investigated to confirm the existence of a Ga-bilayer on top of the GaN structure as the natural termination of the system.

8.3 Outstanding theoretical issues

Throughout this thesis, the CAICISS spectra have been modelled using the FAN simulation software, which offers a choice of the ion-atom interaction potential, with both the ZBL and TFM models available. In the TFM case, the correction factor to the Firsov screening length can also be adjusted. Figure 8.6 shows the data obtained from

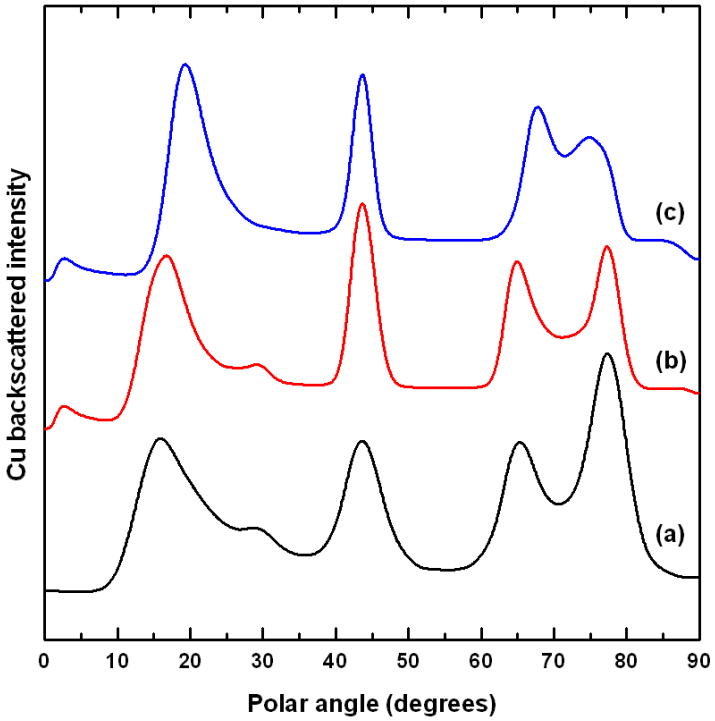

Figure 8.6: (a) The Cu-backscattered intensity profile from the CAICISS data collected in the <110> azimuth from the clean Cu(100) surface. (b) The corresponding FAN simulation result using the TFM potential in conjunction with a screening factor of 0.53. (c) The corresponding FAN simulation result using the ZBL potential.

the clean Cu(100) surface in the <110> azimuth, along with simulations conducted using both the ZBL and TFM potentials. The results clearly indicate that the ZBL potential cannot describe the data from the clean surface to the same degree of accuracy as the TFM potential. This is a somewhat surprising result, with the ZBL potential being a *"universal"* model which should be applicable in all LEIS techniques [90]. However, the TFM potential has been found to be more applicable for larger distances between the shadowing and scattering atoms [219].

As previously presented in equation 3.9, it has been proposed by O'Connor and co-workers [90] that the screening length in the TFM potential can be tuned for each ion-atom combination. A correction factor applied to the screening length changes the width of the shadow cones and hence will alter peak positions in the CAICISS data. Considering some of the surfaces discussed in this thesis and equation 3.9, a correction factor (summarised in table 8.1) of 0.84 should be used for He^+-Ni interactions, 0.85 for He^+-Cu, 0.92 for He^+-In and 1.00 for He^+-Pt. The CAICISS data taken from the clean Cu(100) surface in the <110> azimuth along with simulations using several correction factors is shown in figure 8.7. The results clearly show that a correction factor lower than 0.85 is required, with these data most accurately described using a correction factor of 0.53. The same situation was also observed in the <100> direction. On both the Ni(100) (not presented in this thesis) and Ni(110)-(3×1)-O surfaces, a correction factor of 0.60 was used, again a severe reduction compared to the value of 0.84 predicted by O'Connor. All He^+-Pt interactions were modelled using a correction factor between 0.77 and 0.80, compared to a predicted value of 1.00. Whilst the quality of the InN surfaces studied using CAICISS were not perfect, the structures were modelled reasonably accurately using a correction factor of 0.70, compared to a predicted value of 0.92.

Figure 8.8 shows the predicted value of C_f as a function of atomic number, Z, for the O'Connor correction factor. Also plotted are the four values determined during the work presented in this thesis. It appears that the correction factor for CAICISS experiments may have the same gradient, but the y-axis offset (0.54 in equation 3.9) appears to be incorrect and could be dependent on the mass of the incident ion.

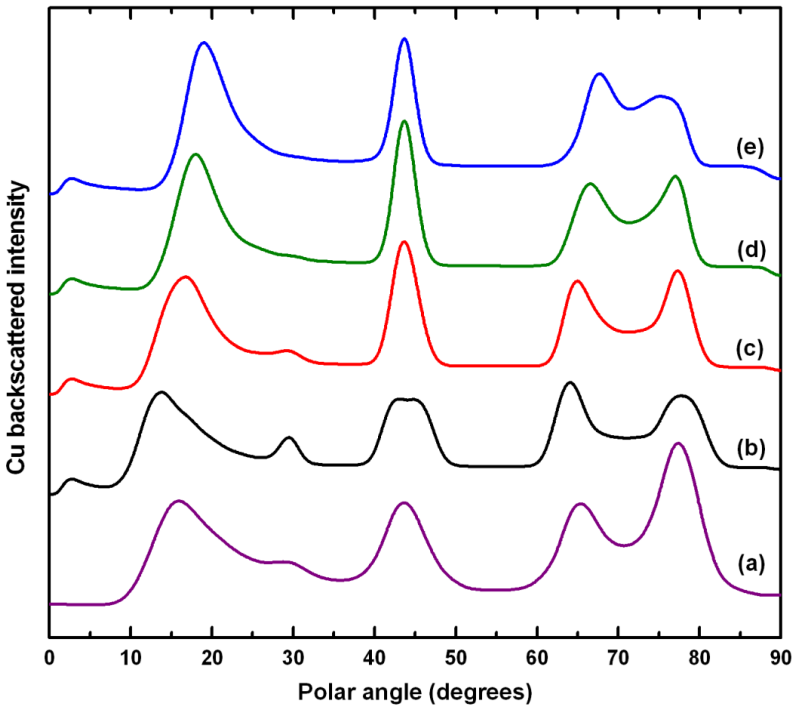

Figure 8.7: (a) The Cu-backscattered intensity profile from the CAICISS data collected in the <110> azimuth from the clean Cu(100) surface. Also shown are the corresponding profiles from FAN simulations using the TFM potential with screening factors of (b) 0.40, (c) 0.53, (d) 0.70 and (e) 0.85 (the value calculated from equation 3.9).

Whilst the correction factor can be determined for each individual experiment, it would be advantageous to have an equation to determine the screening factor prior to the start of analysis of the experimental data. However, values for just four elements are insufficient to propose a new method for determining the correction factor to the Firsov screening length for CAICISS experiments. All data presented were collected with 3 keV He^+ and only four correction factors have been determined. It is essential that further work be carried out on a range of materials (metal single crystals, alloys, semiconductors, etc.) and at a range of incident ion energies to fully investigate the causes of the discrepancy between the values used in this thesis and those calculated using the O'Connor factor.

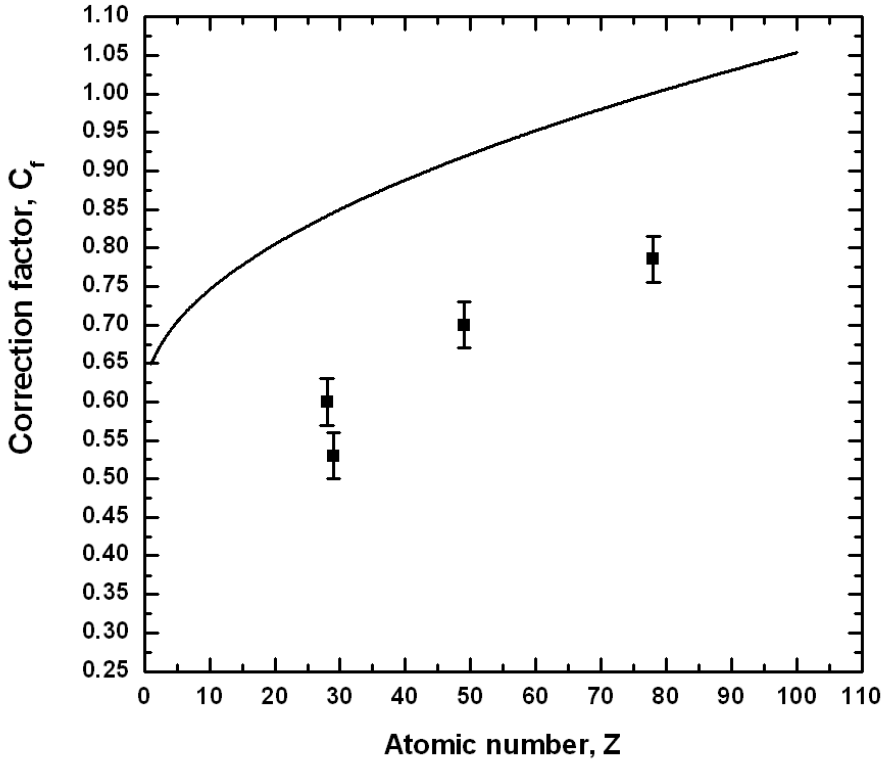

Figure 8.8: The correction factor to the Firsov screening length (C_f) as a function of the target atom mass (Z), calculated from equation 3.9 (solid line). Also shown are the values determined from CAICISS experiments for Ni, Cu, In and Pt (black squares).

Interaction	O'Connor	CAICISS C_f	ΔC_f
He^+-Ni	0.84	0.60	0.24
He^+-Cu	0.85	0.53	0.32
He^+-In	0.92	0.70	0.22
He^+-Pt	1.00	0.78	0.23

Table 8.1: A summary of the expected correction factors to the Firsov screening length from O'Connor *et al.* [90] and values which were employed during analysis of the CAICISS data presented in this thesis. The correction factors determined from CAICISS experiments are accurate to $\pm$ 0.02.

8.4 Proposed improvements to the CAICISS system

Whilst the current experimental setup proved to be adequate for the experiments presented in this thesis, the system could be improved in several areas. The primary area of concern is the characteristics of the ion source and the ion beam within steering section. It has recently been discovered that the ion beam possessed a diameter of approximately 8mm when entering the steering section. This leads to the steering plates having different effects on different parts of the beam. Whilst most of this is filtered out by the final chopping aperture, it does not reflect the ideal situation. To rectify this, a pair of apertures should be installed between the source and the steering section to ensure that a collimated beam with a relatively small diameter ($\sim$ 2 mm) enters the steering section. Also discovered recently was a misalignment within the source itself, which could lead to a slight misalignment of the beam through the lens section of the source. To investigate this, the source should be dismounted and re-aligned. Should the re-alignment fail, steering plates may be required between the source and the first aperture in the new collimating section. An incident beam with optimal properties may enable the observation of lower Z elements such as C and O.

With many surfaces, the current duration of a CAICISS experiment (3 hours) may be problematic in terms of surface contamination. Whilst a re-alignment of the ion source should increase the beam intensity, the new collimating apertures will most likely decrease the overall intensity reaching the sample. To counteract this, the effects of the chopping frequency and the rise time of the chopping electronics should be investigated and improved. With a higher chopping frequency the CAICISS data could be collected within a reduced time frame, with an improved energy resolution. An alternative solution would be to improve the pumping of the main chamber. Pressures in the scattering chamber were often in the 1×10^{-9} mbar region during the experiments. An improvement of at least an order of magnitude should be possible by modifying the pumping system, possibly adding a turbo pump to the main chamber. The need for regular breaking of the vacuum could also be removed by the implementation of a sample transfer mechanism, although care will have to be taken to ensure that the samples can be mounted on to the manipulator in a satisfactory manner.